remote sensing

MDPI

Technical Note

Automated Mapping of Ms 7.0 Jiuzhaigou Earthquake (China) Post-Disaster Landslides Based on High-Resolution UAV Imagery

Rubing Liang [1], Keren Dai [1,2,*], Xianlin Shi [1], Bin Guo [2], Xiujun Dong [2], Feng Liang [1,3], Roberto Tomás [4], Ningling Wen [1] and Xuanmei Fan [2]

1 College of Earth Science, Chengdu University of Technology, Chengdu 610059, Sichuan, China; liangrubing@stu.cdut.edu.cn (R.L.); shixianlin06@cdut.edu.cn (X.S.); liangfeng@stu.cdut.edu.cn (F.L.); wenningling@stu.cdut.edu.cn (N.W.)
2 State Key Laboratory of Geohazard Prevention and Geoenvironment Protection, Chengdu University of Technology, Chengdu 610059, Sichuan, China; guobin@stu.cdut.edu.cn (B.G.); dongxiujun@cdut.cn (X.D.); fanxuanmei2014@cdut.edu.cn (X.F.)
3 Department of Natural Resources of Sichuan Province, Chengdu 610072, Sichuan, China
4 Departamento de Ingeniería Civil, Escuela Politécnica Superior, Universidad de Alicante, P.O. Box 99, E-03080 Alicante, Spain; roberto.tomas@ua.es
* Correspondence: daikeren17@cdut.edu.cn

Abstract: The Ms 7.0 Jiuzhaigou earthquake that occurred on 8 August 2017 triggered hundreds of landslides in the Jiuzhaigou valley scenic and historic-interest area in Sichuan, China, causing heavy casualties and serious property losses. Quick and accurate mapping of post-disaster landslide distribution is of paramount importance for earthquake emergency rescue and the analysis of post-seismic landslides distribution characteristics. The automatic identification of landslides is mostly based on medium- and low-resolution satellite-borne optical remote-sensing imageries, and the high-accuracy interpretation of earthquake-triggered landslides still relies on time-consuming manual interpretation. This paper describes a methodology based on the use of 1 m high-resolution unmanned aerial vehicle (UAV) imagery acquired after the earthquake, and proposes a support vector machine (SVM) classification method combining the roads and villages mask from pre-seismic remote sensing imagery to accurately and automatically map the landslide inventory. Compared with the results of manual visual interpretation, the automatic recognition accuracy could reach 99.89%, and the Kappa coefficient was higher than 0.9, suggesting that the proposed method and 1 m high-resolution UAV imagery greatly improved the mapping accuracy of the landslide area. We also analyzed the spatial-distribution characteristics of earthquake-triggered landslides with the influenced factors of altitude, slope gradient, slope aspect, and the nearest faults, which provided important support for the further study of post-disaster landslide distribution characteristics, susceptibility prediction, and risk assessment.

Keywords: Jiuzhaigou earthquake; landslide mapping; unmanned aerial vehicle imagery; support vector machine; landslide-distribution analysis

Citation: Liang, R.; Dai, K.; Shi, X.; Guo, B.; Dong, X.; Liang, F.; Tomás, R.; Wen, N.; Fan, X. Automated Mapping of Ms 7.0 Jiuzhaigou Earthquake (China) Post-Disaster Landslides Based on High-Resolution UAV Imagery. *Remote Sens.* **2021**, *13*, 1330. https://doi.org/10.3390/rs13071330

Academic Editor: Saeid Pirasteh

Received: 27 February 2021
Accepted: 25 March 2021
Published: 31 March 2021

1. Introduction

On 8 August 2017, an Ms 7.0 earthquake struck Jiuzhaigou County, Sichuan Province, China, with a focal depth of 20 km. The earthquake triggered more than 1000 geological disasters in the Jiuzhaigou valley scenic and historic-interest area, most of which were landslide disasters [1,2]. Although many landslides did not directly threaten the safety of residents' lives and property, they led to serious road damage [3], hindering earthquake emergency rescue work. The rapid and automatic identification of earthquake-triggered landslides is not only helpful for post-seismic emergency-response analysis, but also

of great significance to realize the distribution characteristics of earthquake-triggered landslide disasters for future landslide-susceptibility analysis and disaster reduction [4–6].

Different types of remote-sensing imagery are increasingly used to monitor and identify landslides [7–9]. At present, earthquake-triggered landslides are mainly identified using satellite-borne optical remote-sensing imagery [10,11]. Although satellite-borne optical remote-sensing imagery provides wide coverage and a large spectral range, there are problems such as the long time interval of imagery acquisition, the influence of clouds and fog, and the low spatial resolution, which limit the absolute accuracy of landslide mapping [12,13]. Among them, low spatial resolution is one of the most important conditions restricting the accurate identification of landslides. Unmanned aerial vehicle (UAV) remote-sensing technology, which can quickly obtain high-resolution imageries and provide important data support to analyze the spatial distribution of landslides, is widely used in the mapping of earthquake-triggered landslides [10–21].

From the methodological point of view, the conventional landslide-interpretation methods are mainly based on visual interpretation. Although these types of methods have a high accuracy, they are time-consuming and labor-intensive when interpreting a wide range and large number of earthquake-triggered landslides, and cannot meet the timeliness requirements of earthquake emergency response and rapid assessment [22,23]. In recent years, some scholars have tried to improve the identification efficiency of landslides by using semi-automatic/automatic identification methods, and to establish interpretation signs according to the differences in morphology, texture, and tone of the landslide body to achieve rapid extraction of landslides [24–27]. In the in-depth research on landslide extraction, scholars have found that texture features such as roads and villages are very similar to landslide bodies in remote-sensing imageries, which severely restricts the interpretation results of landslides [4,20]. In order to overcome the above problems, researchers have carried out a number of explorations. Chen et al. [28] introduced three basic shapes commonly seen in landslides as a screening for landslide bodies, so that the classification accuracy of landslides was improved. Liu et al. [29] added three new layers (i.e., digital surface model, slope gradient, and slope aspect) to limit the distribution of landslides based on the original three RGB bands, so as to better distinguish the impact of roads and villages on landslides. These methods have achieved results that are certain and promoted the development of accurate landslide-identification research. However, these kinds of methods still require human intervention and do not completely achieve automatic identification. The accuracy of landslide identification is about 90%, and the results are still affected by roads and villages. With the development of ultrahigh-resolution UAV imagery, the high-precision automatic identification of landslides based on UAV imagery at a high-resolution scale of one meter or less is worthy of further studying.

This study uses high-resolution UAV remote-sensing imagery and proposes a support vector machine/UAV imagery method for automatic landslide identification that incorporates pre-seismic image-recognition results for masking. This method selects roads, villages, and landslides as the feature vectors of the samples; constructs a support vector machine automatic-recognition method that mixes imagery features such as spectrum, color tone, and texture, etc.; extracts distribution information through imagery comparison before and after earthquake; eliminates the extraction errors caused by the interpretation results of roads and villages; and then realizes the accurate identification of landslides. At the same time, high-resolution digital elevation model (DEM) data and fault data are introduced to carry out statistical research on the spatial distribution characteristics of earthquake-triggered landslides, which provides important support for susceptibility and risk assessment.

2. Study Area and Data Sets

The Jiuzhaigou valley scenic and historic-interest area is located in Zhangzha Town, Jiuzhaigou County, in the northwestern Sichuan Province, in the northeast side of Gongganling in the southern section of Minshan Mountai, more than 400 km away from Chengdu.

The altitude of the north edge is 2000 m above sea level, while the altitude of the south edge is more than 3700 m above sea level (Figure 1). Due to the deep valleys and the large difference in altitude, the main landform types are high mountains and deep valleys. Several faults (i.e., Tazang Fault, Minjiang Fault, Dongmengou Fault, Huya Fault, and Yifu Fault [16,30–32]) are located near the study area. Affected by the Ms 7.0 earthquake on 8 August 2017, the loose materials on the surface of the slope in the study area have a large sliding component along the contact surface, and the poor stability of the slope facilitated the development of many earthquake-triggered landslides [33]. According to data from the China Earthquake Network Center, this earthquake caused 25 deaths, 525 injuries, and 6 disappearances; 176,492 people were affected, and 73,671 houses were damaged to varying degrees [34]. This not only caused great damage to the tourist resources and ecological environment of the scenic area, but also caused a great impact on the local residents.

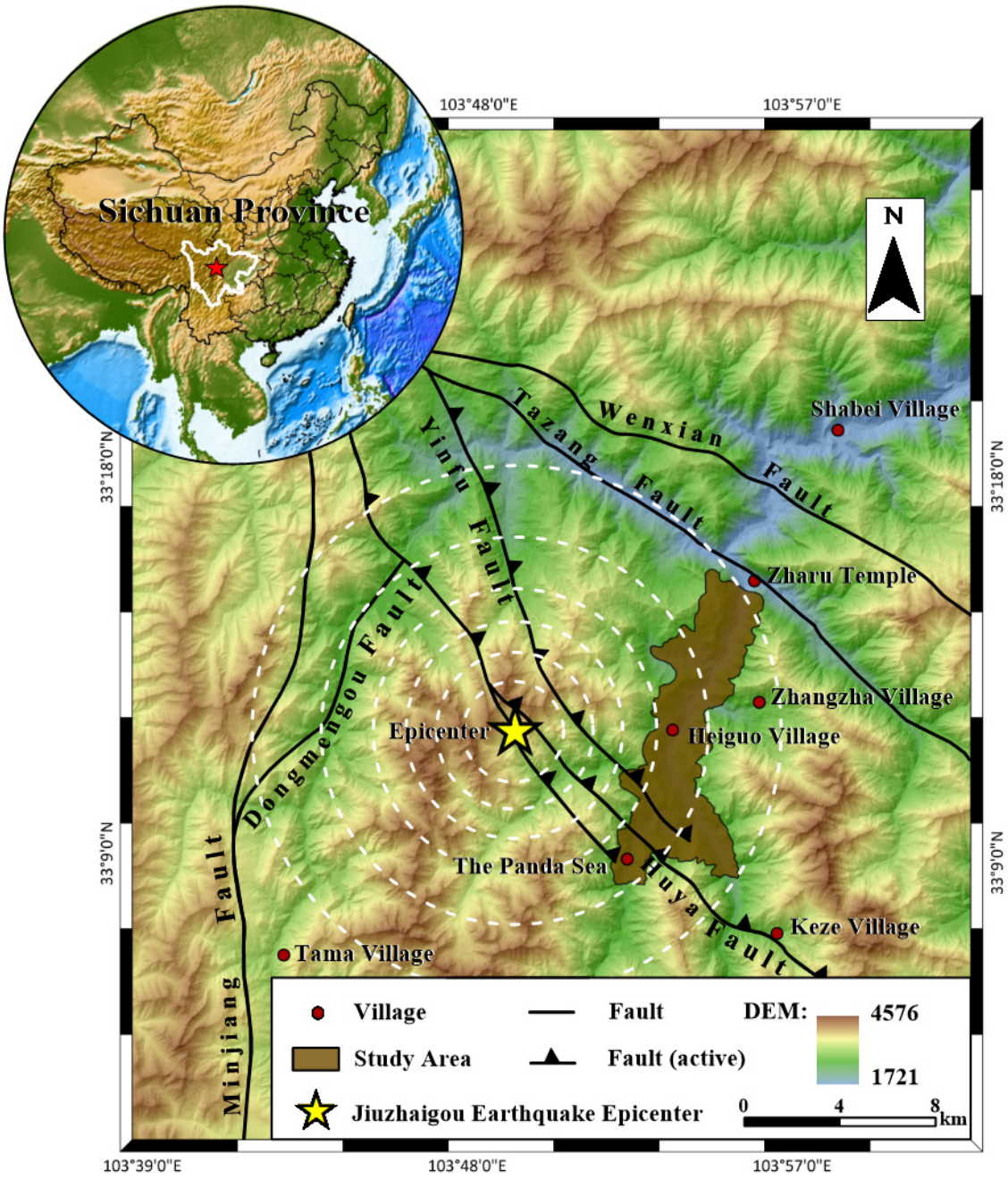

Figure 1. Location and maps of the study area. DEM height in m above sea level.

The satellite-borne optical remote-sensing imageries obtained after the earthquake in the Jiuzhaigou valley scenic and historic-interest area were greatly affected by clouds and fog, and did not enable full interpretation of the damage. UAV imageries have the advantages of strong maneuverability and high spatial resolution, which can make up for the lack of effective imaging of spaceborne imageries, and cover places unreachable by people. They have been widely used in geological environment and disaster investigation, post-seismic emergency response and disaster assessment, and other fields [35,36]. On 12 August 2017, four days after the earthquake, our research team carried out a UAV flight (Huaao X-UAV) to obtain optical imagery and high-resolution DEM data after the earthquake in the Jiuzhaigou valley scenic and historic-interest area (Figure 2B). The imagery covered 4.03×10^7 m^2, and the spatial resolution sampling was 1 m (Figure 2B). A SPOT5 remote-sensing imagery acquired on 21 October 2015, with a resolution of 2.5 m was also used (Figure 2A). Some photos (Figure 3) were taken during our field investigation on 5 July 2019, in which the wide-distribution landslides were confirmed. From the comparison of the satellite-borne remote-sensing imagery before the earthquake and the UAV imagery after the earthquake (Figure 2), it can be seen that there were a large number of landslides in the study area, and their distribution was wide and dense in some areas, but the scale of landslides was mainly small and medium, and there was no large-scale damage.

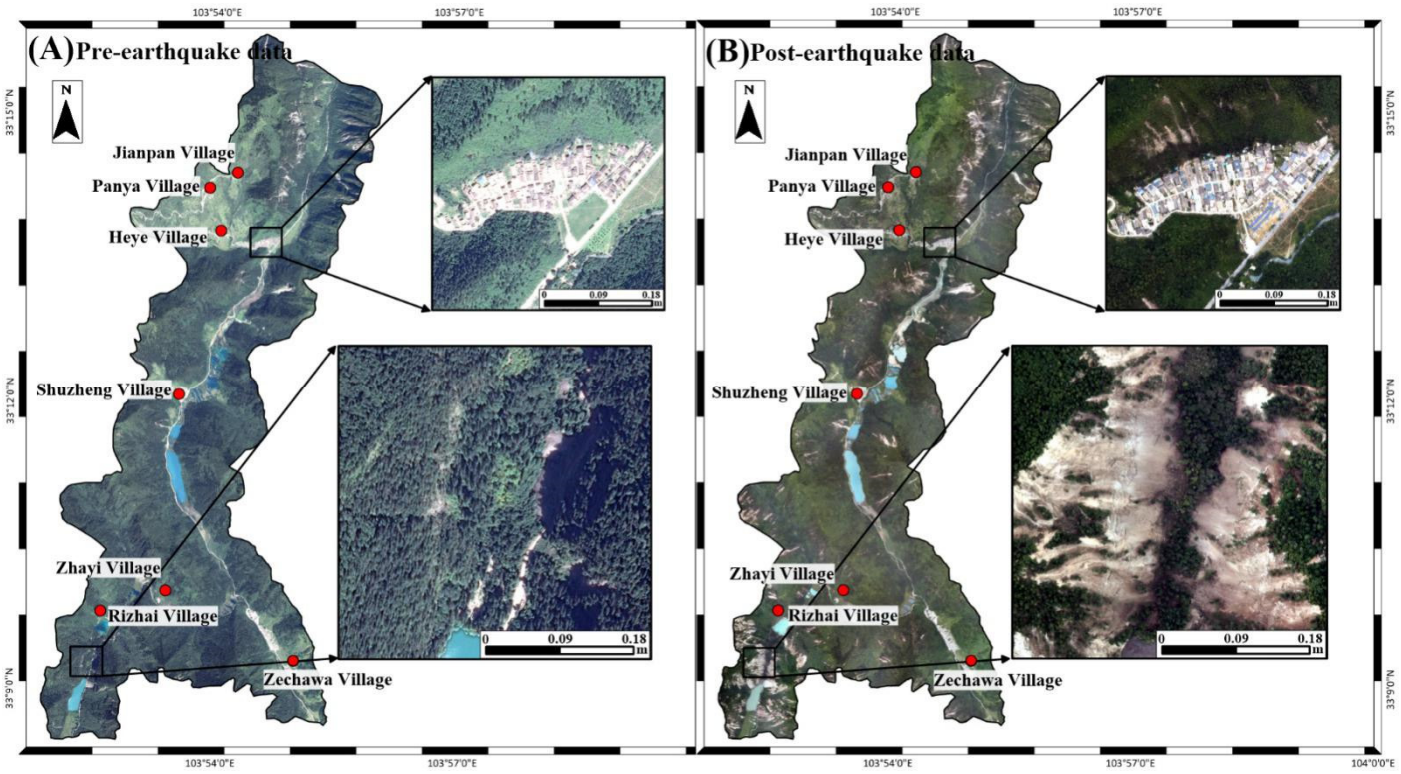

Figure 2. (**A**) Space-borne optical remote-sensing imagery before the earthquake, with a resolution of 2.5 m; (**B**) UAV imagery after earthquake, with a resolution of 1 m.

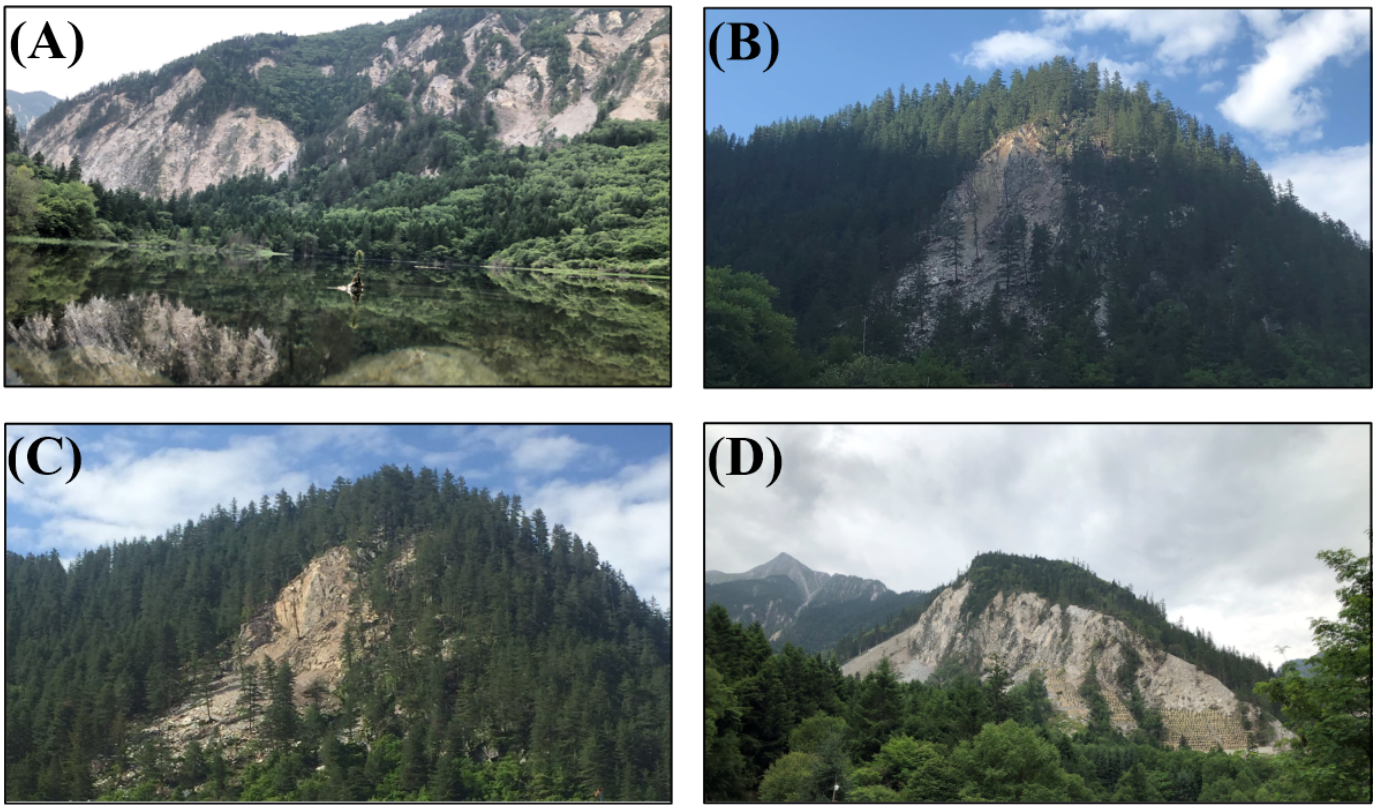

Figure 3. (**A**–**D**) Onsite photos of some areas affected by landslides taken during our field investigation of the Jiuzhaigou valley scenic and historic-interest area on 5 July 2019.

3. Methodology

This paper proposes a support vector machine automatic-recognition method that mixes imagery features such as spectrum, tone, texture, etc., and extracts landslide distribution information by comparing imageries before and after earthquakes. The support vector machine classification method is a classic machine-learning classification technique based on Vapnick–Chervonenkis (VC) dimensional theory and structural-risk minimization, which have important applications in imagery processing and target recognition [37,38]. This is a supervised learning method that uses the category information of known training points to find the correspondence between the points to be verified and the types, separates the training set by category, and predicts the relationship corresponding to the new training point [39]. It can largely solve the shortcomings of traditional methods (such as neural networks) without causing the Hughes phenomenon, which indicates that for limited training samples, the classification accuracy decreases as the feature dimension increases [40]. Since the spectral values of the various categories in UAV imageries are relatively close, the use of a support vector machine classification method to identify landslides can avoid the phenomenon of "same objects with different spectrum, different objects with same spectrum", and improve the classification accuracy of remote-sensing imageries [41].

The support vector machine classification method captures the target through the difference of spectrum, tone, and texture; and converts the recognition of the sample target in the imagery into the optimal hyperplane problem in the high-dimensional feature space, which is equivalent to solving the following equation:

$$min\varphi(\omega) = \frac{1}{2}(\omega \cdot \omega) + C(\sum_{i=1}^{l} \xi_i) \quad (1)$$

$$s.t.y_i[(\omega \cdot x_i) - b] \geq 1 - \xi_i, i = 1, 2, l \quad (2)$$

The RGB value in the panchromatic band, $y_i = (-1, 1)$, is the sample classification label; C is the multiplication coefficient; and $\xi = (\xi_1, \xi_2, \cdots, \xi_l)$ is the slack variable. Solving Equations (1) and (2), we can get the discriminant function of the support vector machine classification:

$$f(x) = sgn(\sum_{i=1}^{l} y_i \alpha_i^0 K(x, x_i) - b^0) \quad (3)$$

Among these, $K(\cdot)$ is the kernel function that satisfies the Mercer's condition.

Because of roads, villages and fresh landslides have similar texture features, so direct classification of them will cause inevitable misclassification, which is also the current difficulty in earthquake-triggered landslides identification. Therefore, this study uses pre-seismic remote-sensing imagery as auxiliary data, selects road and villages as the feature vectors of the samples, and constructs a support vector machine classification method to train and classify the samples. The classification result is restricted by the model type, kernel function, and loss function, and the reliability of the result is judged by calculating the model prediction error, and the result with larger error is reclassified. When the result error is relatively reliable, the classification result at this time is converted into vector data for output (Figure 4A).

In the space-borne optical remote-sensing imagery before the earthquake, it can be seen that the vegetation in the Jiuzhaigou valley scenic and historic-interest area is densely covered, a small amount of rock avalanches are distributed at the northern end of the study area, and there are almost no clear landslides (Figure 5A). It can be seen in the detailed map (Figure 5B–E) that the road and villages in the study area are well identified by the space-borne optical remote-sensing imagery before the earthquake, laying the foundation for the identification of landslides after the earthquake. The existence of villages can be seen in the images of areas B and E, and there are no traces of landslides and rock avalanches around. However, there are small-rock avalanches in areas C and D (Figure 5C,D), which may be related to the occurrence of the previous earthquake.

Next, the proposed procedure masks the pre-seismic classification results of road and villages on the UAV imagery (acquired after the earthquake). Thus, after excluding road and villages, the post-seismic imagery was used for landslides extraction. Due to the destruction of vegetation on the surface by the landslides, the rock and soil below are exposed, and the imagery appears as light tones and off-white tones. Landslide bodies that are still occurring or have just occurred exhibit strong reflectivity to the spectrum because their exposed parts are mostly fresh structural surfaces. This makes the imagery appear light-toned, and the contrast with surrounding objects is obvious. Therefore, the landslide samples were selected based on the above landslide characteristics, using the support vector machine classification method to train the samples again, extract the landslide classification results after the earthquake, and perform error analysis. When the error is small, the landslide results at that time will be considered as the final result (Figure 4B).

The last step consists of the development of the statistical analysis of the landslide-classification results. First, area statistics for the extraction results of the landslide are determined; then the accuracy of this method combined with visual interpretation of the landslide results is evaluated; finally, the high-resolution DEM and fault data are considered to analyze the current status of the landslides distribution after the earthquake. This paper selects four common topographical factors: elevation, slope gradient, slope aspect, and distance from faults, to obtain the topographic characteristics of the landslides by statistics to find the law of the spatial distribution of earthquake-triggered landslides in the terrain, and to provide an important reference for earthquake-triggered landslide susceptibility and risk evaluation (Figure 4C).

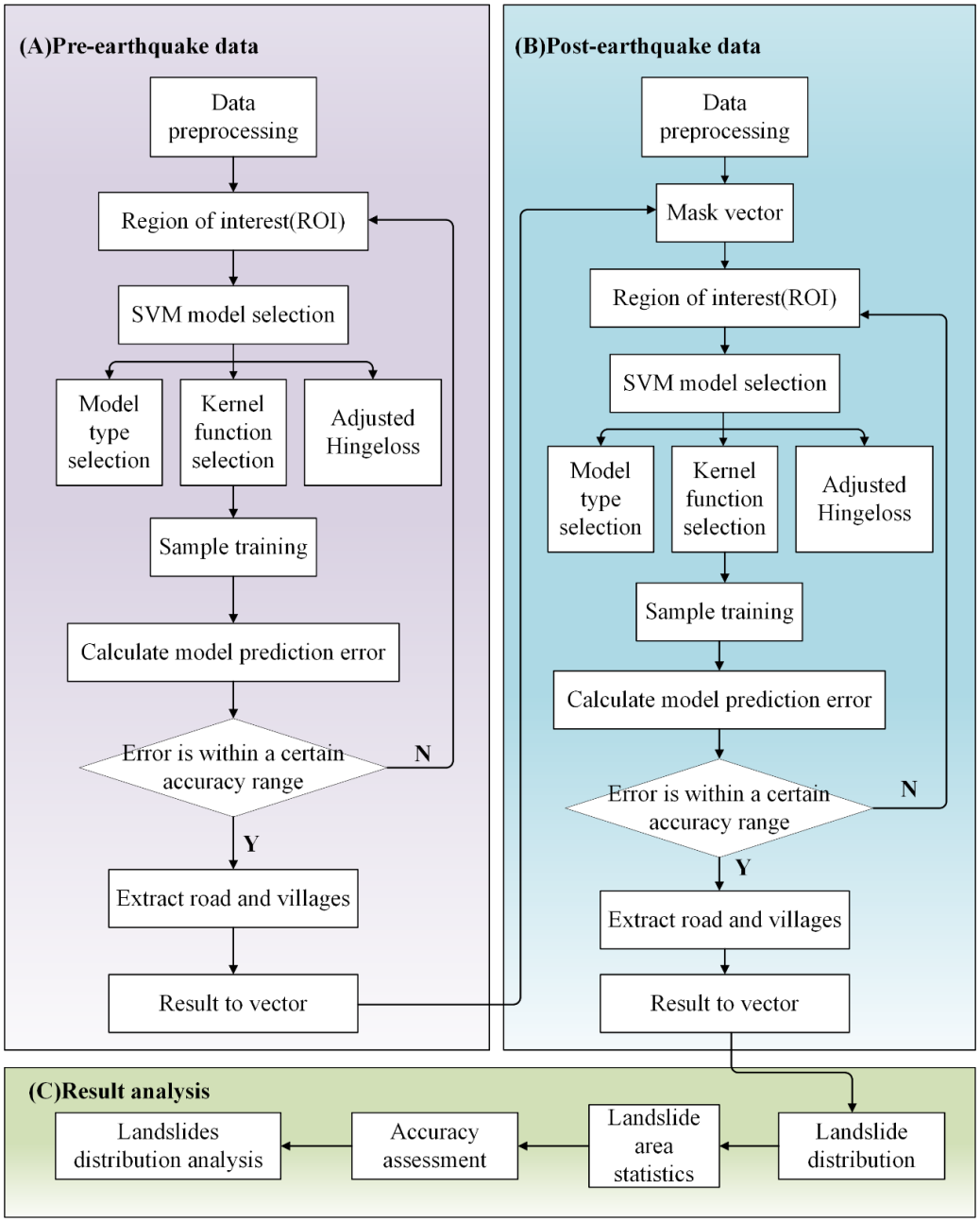

Figure 4. Flow chart of the proposed support vector machine classification method with imageries before and after earthquakes and spatial feature analysis. (**A**) Extracting roads and villages by pre-earthquake imagery; (**B**) extract landslides by post-earthquake imagery; (**C**) The statistical analysis of the landslide distribution.

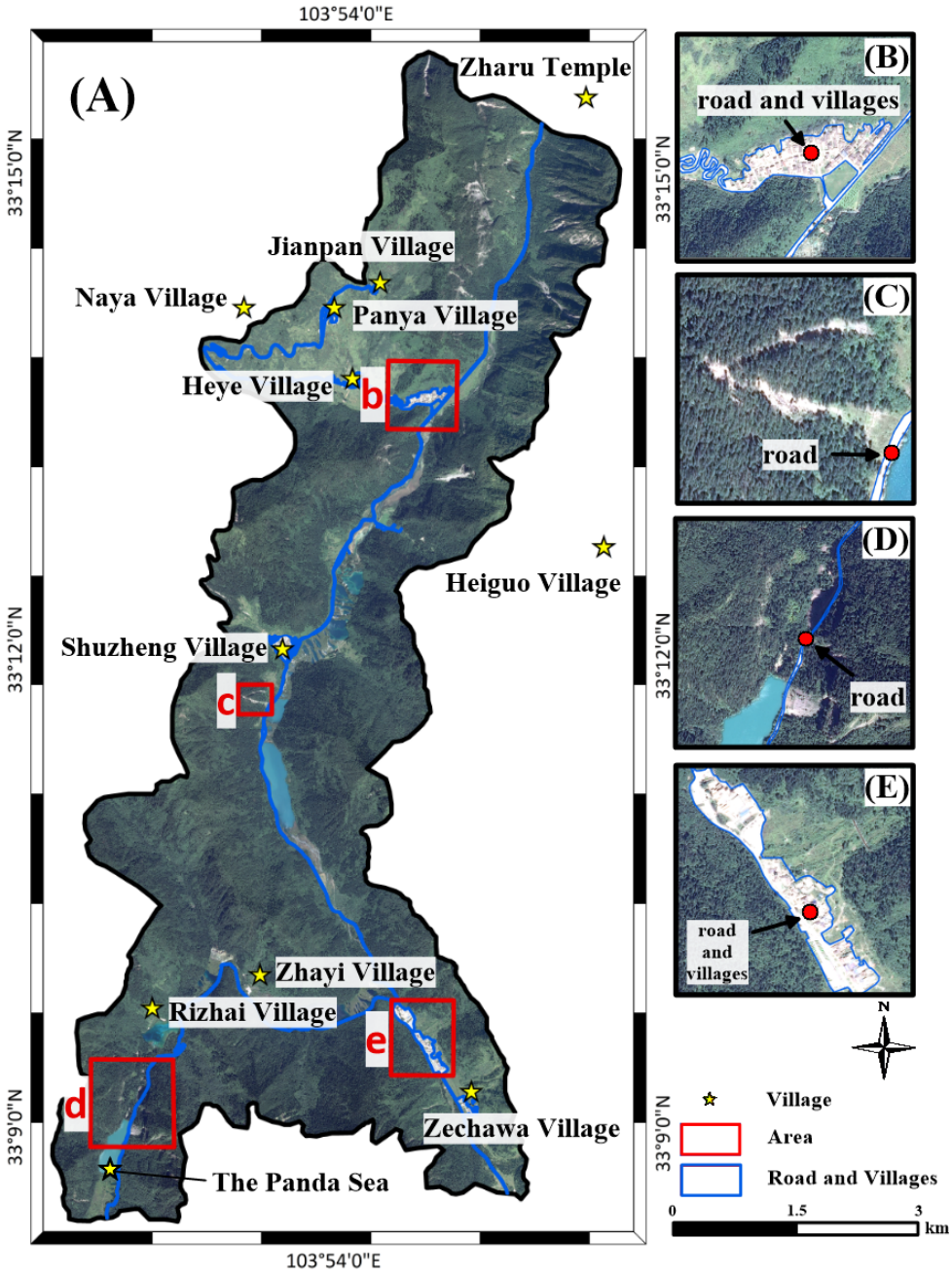

Figure 5. (**A**) Space-borne optical remote-sensing imagery before the earthquake, with the identification results of roads and villages; (**B**–**E**) typical details of the region.

4. Mapping the Post-Disaster Landslides

Using the method proposed in this study, the errors caused by roads and villages were eliminated based on the comparison of the remote-sensing imageries before and after the earthquake. Automatic extraction of the earthquake-triggered landslides was achieved. An accumulated landslide volume of 2.17×10^6 m^2 was identified in the Jiuzhaigou valley scenic and historic-interest area. The landslides were widely and unevenly distributed in the study area with local concentration. The slopes near the Panda Sea received the most serious damage (Figure 6A). In order to further illustrate the advantages and disadvantages of this method, four typical areas were selected for detailed description. The selection of typical areas follows the principle of being close to road and villages, and was evenly distributed in the identification area to better illustrate the extraction of landslides at different locations. The test area B (Figure 6B) is located at the northwest of the study area, at the lower right

of the Heye Village, where the landslides can be well distinguished. However, due to the presence of landslide mass deposition, some non-landslide parts were also circled by the classifier, appearing as dots distributed around the landslide body. The test area C (Figure 6C) is located at the west of the study area, at the bottom left of the Shuzheng Village. The landslides in this area were distributed in multiple blocks. The roads were masked by the pre-seismic imagery-recognition results, which can be well distinguished from the landslide body. The test area D (Figure 6D) is located at the southwest of the study area, near the Panda Sea. Landslides were concentrated and distributed in this area, with a large number covering a wide area. Part of the slide sediment facies slipped into the Panda Sea Lake; these were also identified by the classifier as landslides. The test area E (Figure 6E) is located at the southeast of the study area, to the left of the Zachawa Village. The landslides were less distributed in this area, and most of them were the traces of debris flows.

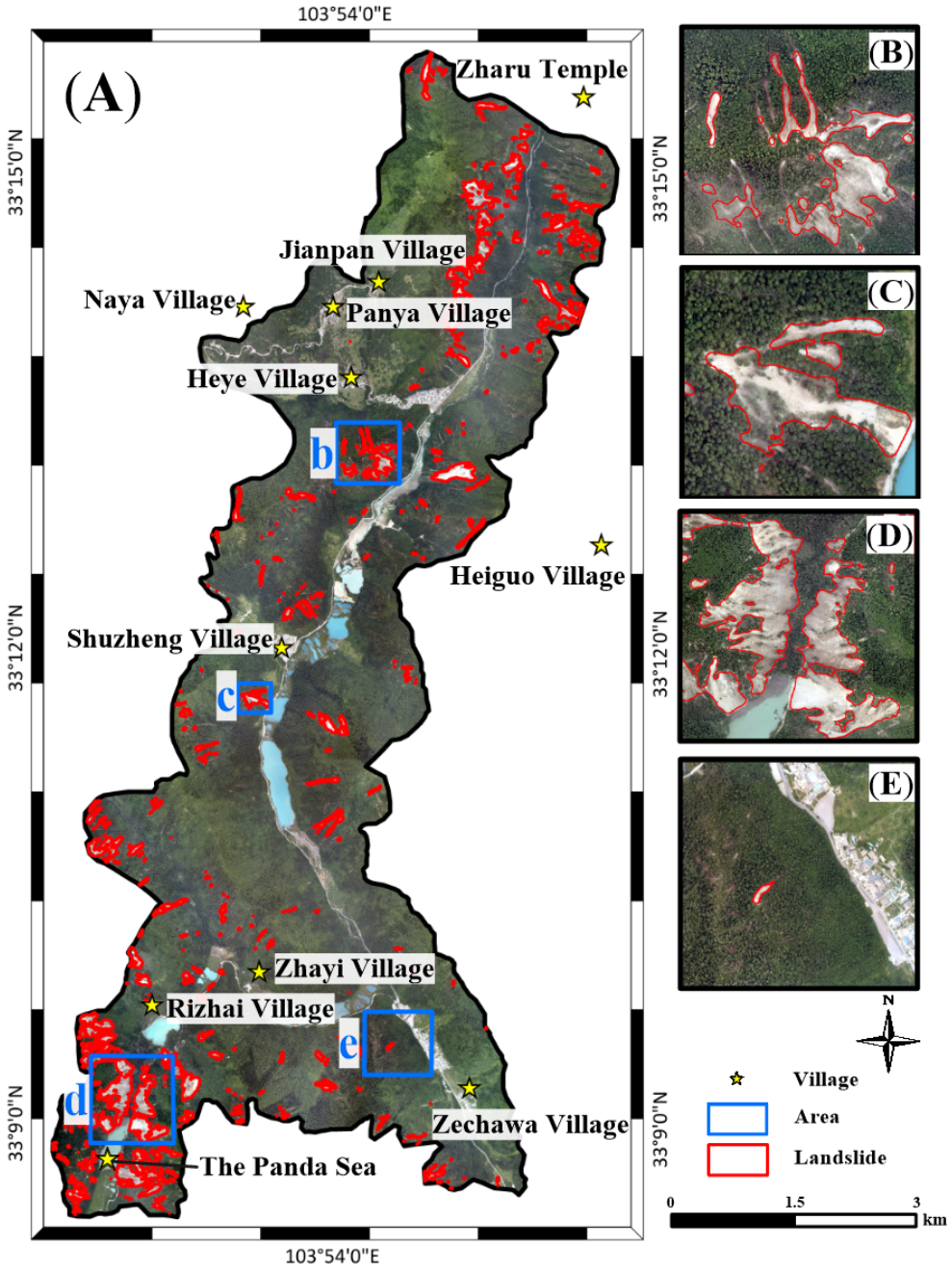

Figure 6. (**A**) Distribution of landslides in UAV imagery after the earthquake. (**B**–**E**) Details of typical regional landslide distribution. Red contours delineate the location of the landslides.

The reliability of disaster identification results is very important for earthquake emergency rescue. In order to quantify the comparison of the accuracy of landslide identification, visual interpretation was used to accurately identify earthquake-triggered landslides as a comparison to verify the true value. This paper introduces a confusion matrix to calculate user's accuracy (UA), commission error (CE), omission error (OE), producer's accuracy (PA), overall accuracy (OA), and the Kappa coefficient to evaluate the accuracy of this method (Table 1). Among them, overall accuracy and the Kappa coefficient are global indicators to measure the accuracy of the classification. The former is defined as the percentage of correct samples, including background and objects; the latter is an evaluation indicator for measuring good or bad, used to measure classification accuracy [42]. Commission error refers to being classified into a class of interest, which actually belongs to another type of pixel; omission error refers to a true classification of the ground surface, but not being classified into the corresponding class by the classifier.

Table 1. Accuracy analysis of landslide-identification results.

Class	PA%	UA%	OA%	Kappa	CE%	OE%
Landslide	99.89	69.17	99.89	0.9117	30.83	0.11

The overall accuracy of automatically extracting landslides in the study area using the support vector machine classification method was 99.89%, which is high. Verification based on visual interpretation results confirmed that this method could eliminate the misclassification caused by the collapse of the landslide body and the similar tones of the road, the village, and the landslide body, and improved the landslide-recognition results. However, there were still some landslides that fell into the lake to form a barrier lake, which led to misclassification of the lake part during the identification process, resulting in an increased commission error. At the same time, this method eliminated all road areas, which made it impossible to identify the parts of the roads that were concealed after the earthquake landslide, resulting in an increase in the omission error.

This paper selected four typical areas as the research test areas (Figure 7), quantitatively compared the difference in the area of landslide identified by the two methods (i.e., the proposed automatic method and visual interpretation) in the test areas, and analyzed the results. Test area A (Figure 7A) is located at the northwest of the study area, below the Heye Village, and was affected by small-scale slides covering most of the area. The area of landslide automatically identified by this method in this test area was 8.12×10^4 m^2, and the area of landslide identified by visual interpretation was 9.39×10^4 m^2; the difference was 1.27×10^3 m^2 and the accuracy was 86.44%. Test area B (Figure 7B) is located at the west of the study area, below the Shuzheng Village. This zone was mainly affected by small-scale slides. There were fewer landslides in this area, but one of them was large. The area covered by the landslides identified by this method in test area B was 2.83×10^4 m^2, and the area of landslide identified by visual interpretation was 1.80×10^4 m^2; the difference was 1.03×10^4 m^2 and the accuracy was 63.59%. Test area C (Figure 7C) is located at the southwest corner of the study area, near the Panda Sea. The main type of landslides in this area were medium-sized. The large number of landslides were distributed in blocks, covering a large area, making it one of the most severely affected areas in the earthquake. The area of landslide identified by this method in test area C was 3.29×10^5 m^2, and the area of landslide identified by visual interpretation was 3.21×10^5 m^2; the difference was 8.16×10^3 m^2 and the accuracy was 97.52%. Test area D (Figure 7D) is located at the left side of the Zechawa Village, to the southeast of the study area. The main type was small-size slides, and landslides were scattered in this area. The area of landslide identified by the automatic method and by visual interpretation in test area D were 2.11×10^3 m^2 and 1.96×10^3 m^2, respectively. The difference was 1.52×10^2 m^2 and the accuracy was 92.77%.

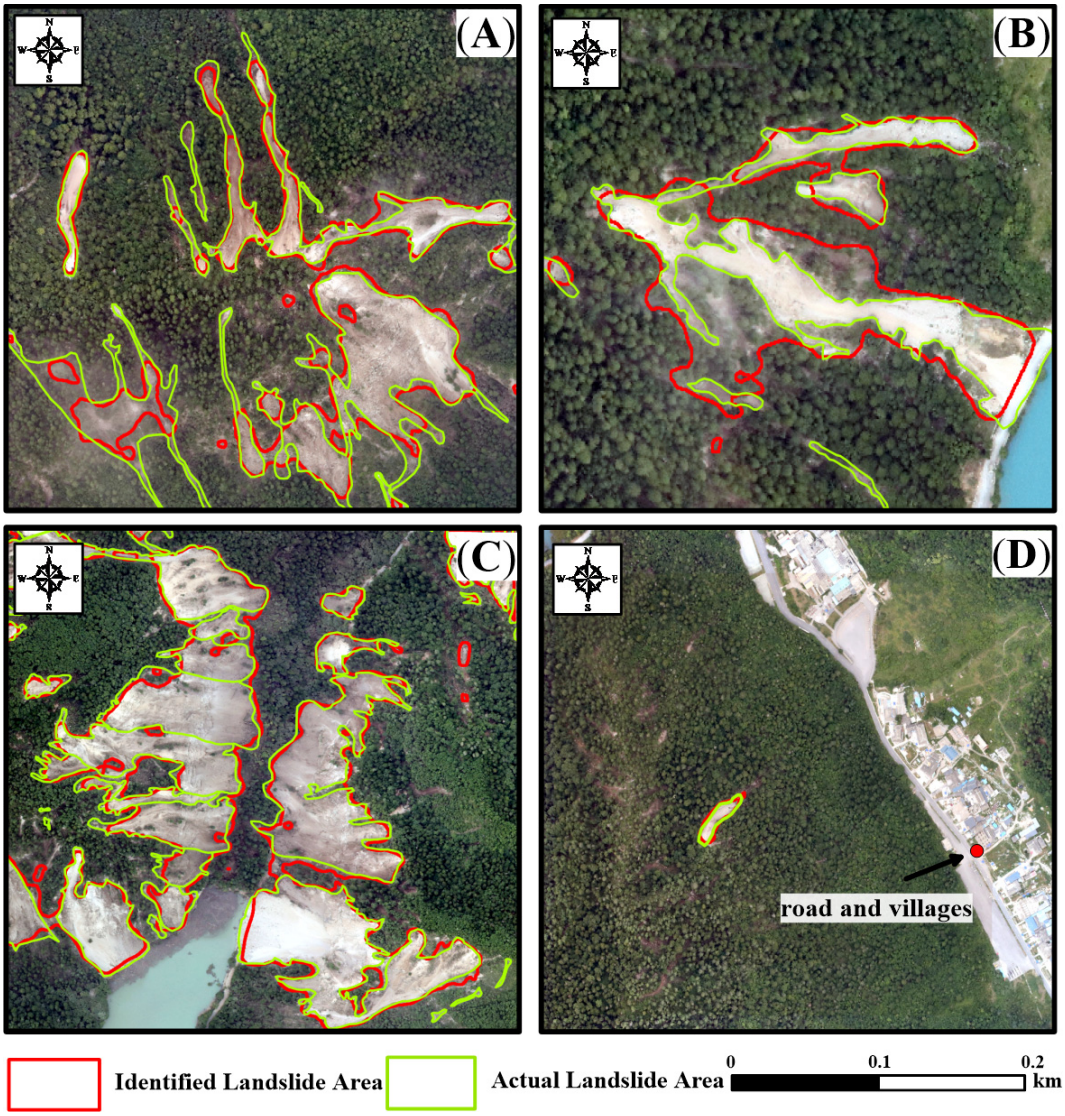

Figure 7. Comparison of identified and actual landslide contours (by visual interpretation) in the four test areas.

The differences observed in the estimation of the landslide identified by the two methods were mainly due to the presence of small-rock avalanches. The occurrence of earthquake-triggered landslides was accompanied by the generation of rock avalanches, which moved from a high altitude to the valley area, leaving a grayish-white tone similar to the landslide body on the UAV imagery, which made it impossible to remove the landslide during the extraction process, and increased the extraction area of the landslide. According to the high-resolution imageries of the four typical areas, it can be seen that although the texture features of road and villages were similar to the landslide body, the confusing areas could be eliminated well by introducing pre-earthquake data as the mask. The accuracy of the landslide recognition result was high, which verified the feasibility of this method.

5. Landslide-Distribution Analysis

Earthquake-triggered landslide disasters are mainly controlled by three types of factors: inducing (earthquake), geological, and topographic [43]. Among these, the inducing factors are mainly due to the deformation of the ground surface and the loosening of mountain deposits caused by seismic motion; the inertial force of the slope body changes, which destroys the original balance of the landslide body, thereby causing the landslide body to slide down or flow. In terms of geological factors, the strength of the seismic wave exceeds the strength of the rock mass or the soil during the propagation process, causing the failure

of the rock mass or soil in the slope. The fallen and accumulated material adheres to the loose deposits below and pushes the loose deposits down, thereby forming a landslide [44]. Topographic factors are important conditions for gestation of landslides. Statistical analysis of topographic factors can obtain the topographic characteristics of landslides, and then dig out its distribution law. The results can provide important reference and guiding significance for secondary earthquake disaster-risk assessment, urban zoning, disaster prevention and mitigation, etc. [45]. The first two factors are well explained by other scholars. This study mainly analyzed the influence of topographic factors on earthquake-triggered landslides, and carried out statistical research on the spatial distribution of earthquake-triggered landslides.

Based on geographic information system (GIS) technology, and according to the high-resolution DEM data obtained by a UAV aerial survey and existing fault data as the data source, the spatial-analysis function of GIS is used to calculate the statistical relationship between elevation, slope gradient, slope aspect, and distance from fault, as well as landslide distribution.

The statistical histogram obtained using the cross analysis of elevation, derived from the DEM, and induced landslides is shown in Figures 8A and 9A. The earthquake-triggered landslides were mainly distributed in the range of 2400–3000 m above sea level. The landslides area in this zone was 1.32×10^6 m^2, accounting for 60.83% of the total landslide disaster area. Among them, the area density was the highest in the elevation range of 2400–2600 m above sea level, and the landslide area was 5.02×10^5 m^2, accounting for 23.13% of the total landslide disaster area. The earthquake-triggered landslides area outside this range were significantly reduced. The reason for the distribution of this landslide was due to the large difference in elevation in the area, the steep and gentle boundary of the slope, and the special topographical conditions that were conducive to the generation of the mountain's free surfaces. The action of the earthquake made the sliding component of the free surface larger, which made the slope unstable and aided the formation of earthquake-triggered landslides.

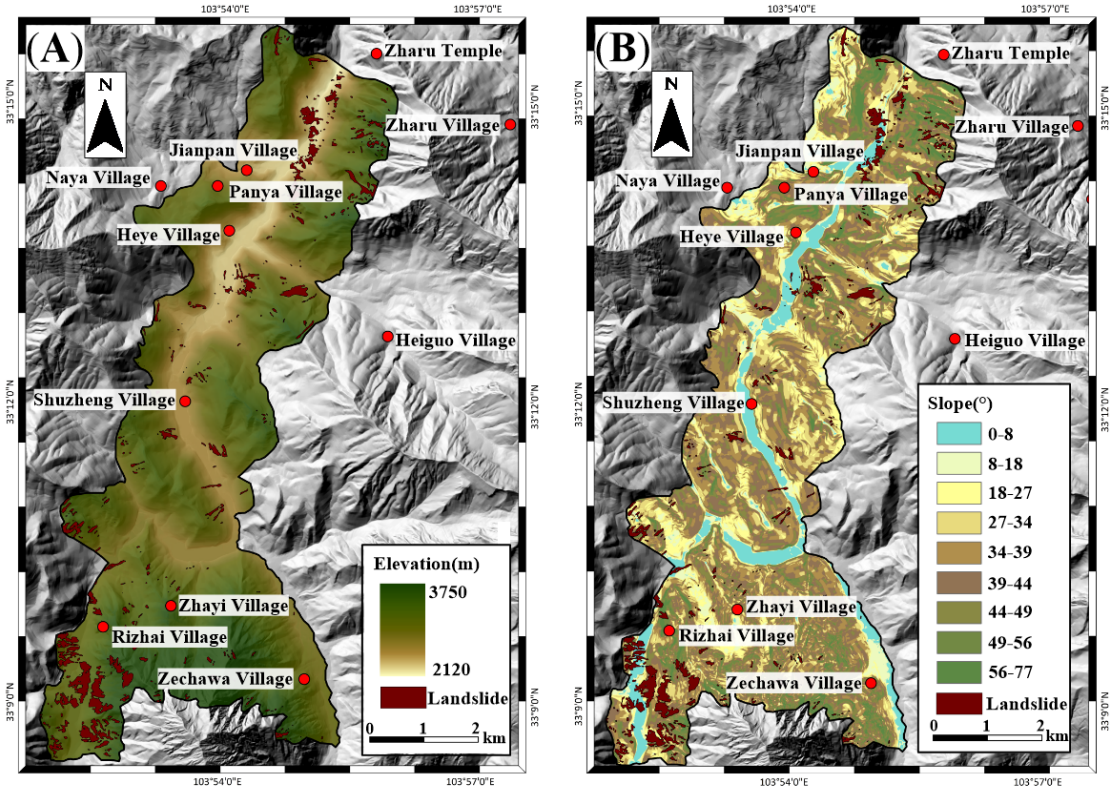

Figure 8. *Cont.*

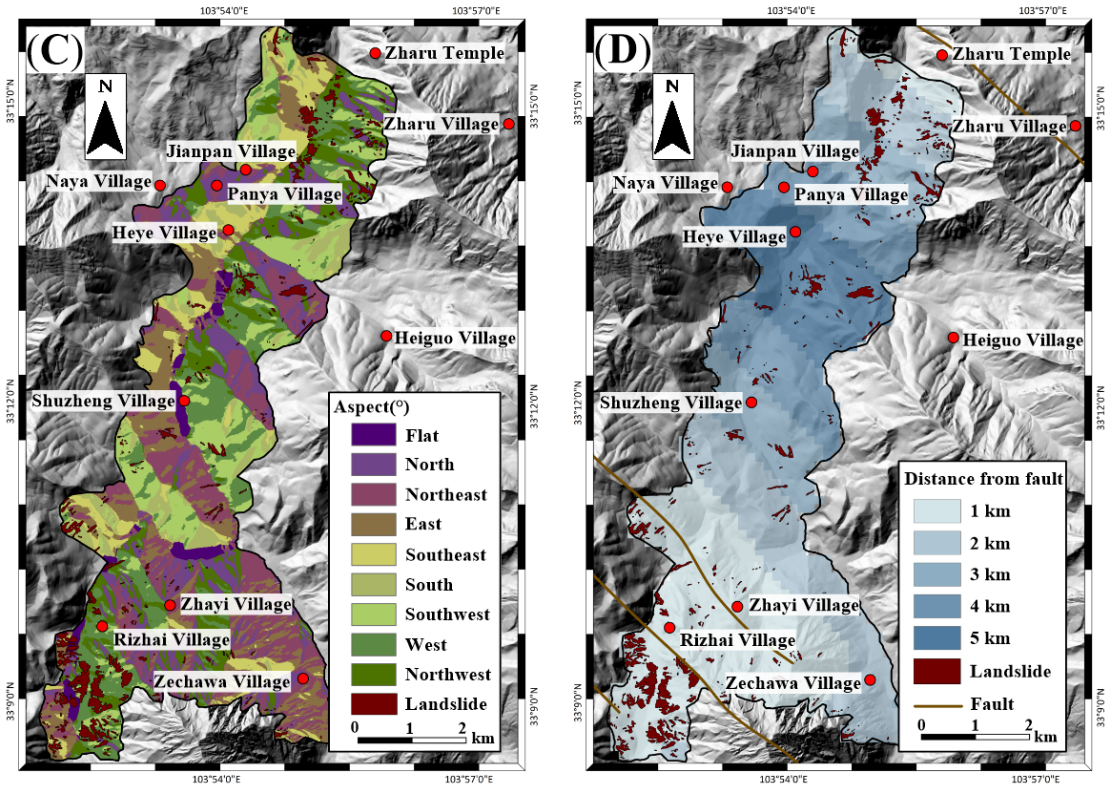

Figure 8. Maps of evaluation factors for the Jiuzhaigou earthquake-triggered landslides: (**A**) elevation; (**B**) slope gradient; (**C**) slope aspect (topographic); (**D**) distance from fault.

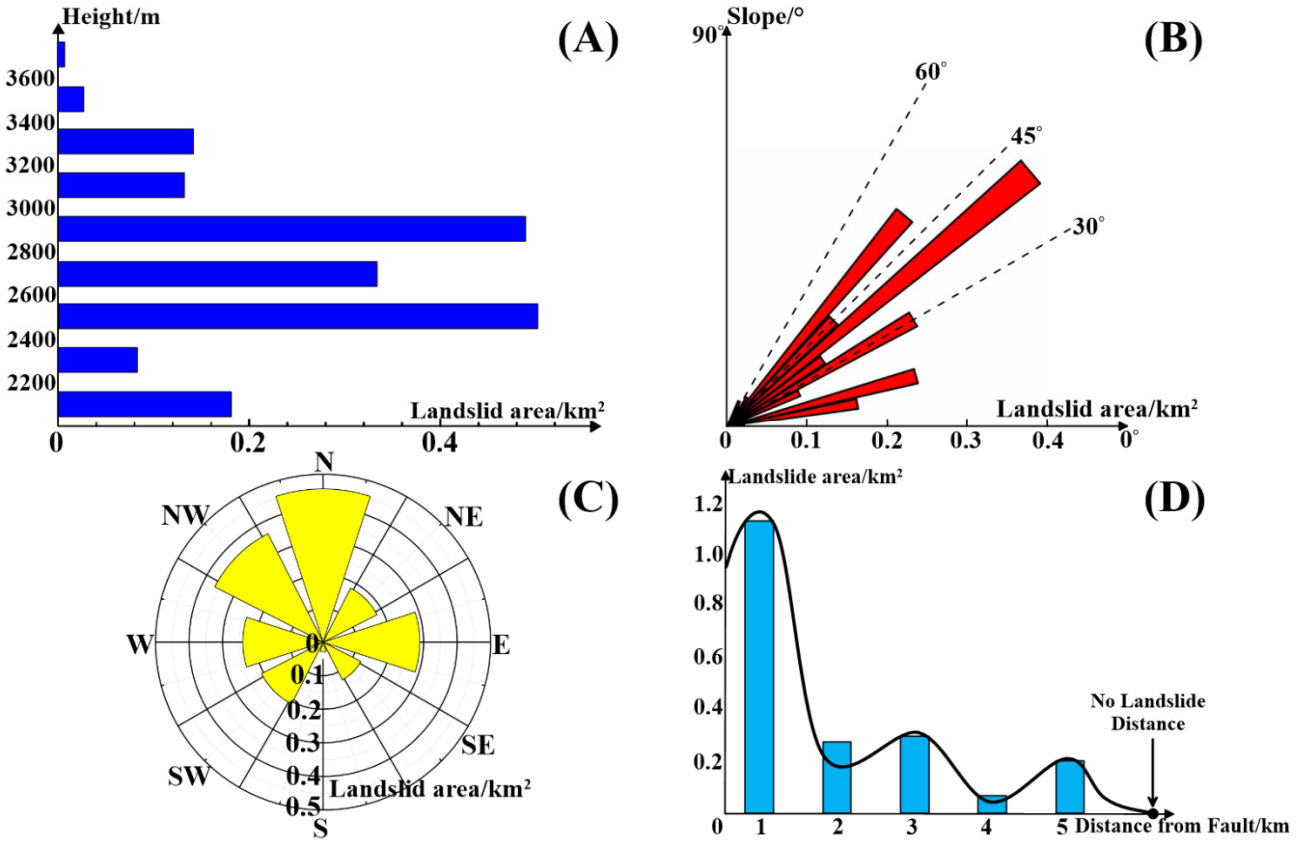

Figure 9. Statistical histogram of evaluation factors of earthquake-triggered landslides: (**A**) elevation; (**B**) slope gradient; (**C**) slope aspect; (**D**) distance from fault.

Slope gradient is an important factor affecting the occurrence of landslides. Previous statistical studies have shown that earthquake-induced geological disasters mostly occur in the range of 20~50° [43]. For example, the landslide disasters induced by the Eastern Iburi earthquake in Hokkaido, Japan, mostly occurred in the range of 20~30° [46,47]. As shown in Figures 8B and 9B, the slope gradient of the landslides in the study area were mainly distributed in 35~40°, and the area of the landslides for this range was 4.54×10^5 m^2, which accounts for 20.92% of the total landslide area. The main reasons for the landslides in this area were inseparable from the influence of the steep topography. The research results were in line with the range of slope gradients that are prone to geological disasters, and corresponded with the existing research results.

The slope aspect effect of an earthquake-triggered landslides is determined by seismic factors [2]. Xu and Lie [48] found in their study of the Wenchuan earthquake disaster that the distribution of landslides in the slope direction was affected by the seismic wave propagation and the faulty action of the fault zone, which manifested as "backslope effect" and "dislocation". To a certain extent, this discovery can provide a basis for the location of the seismogenic fault to a certain extent. Landslide disasters in the study area were concentrated in the northern slope direction (Figures 8C and 9C), with an area as high as 4.57×10^5 m^2, accounting for 21.06% of the total landslide area. Through further research, a relationship between the spatial distribution of the landslides and the slope aspect was not found. It was speculated that it was the reason why the study area was far away from the earthquake fault, and it may also have been affected by the smaller number of landslides.

Earthquake-triggered landslides are controlled by active faults, and the spatial distribution of landslides has a certain relationship with the distance from seismogenic faults. Dai et al. [16] found that most of the earthquake-triggered landslides in the study area were distributed along the northwest–southeast directions, and their number increased with the decrease of the distance from the fault, which had an obvious fault effect. The geological structure of the study area is complex, and there are two faults passing through the scenic spot, and two other faults are located nearby. The dense faults caused the development of earthquake-triggered landslides in the study area [30]. Therefore, this study used the ArcGIS spatial-analysis function to analyze the Euclidean distance of the fault data to calculate the area of earthquake-triggered landslides within different distances (Figures 8D and 9D). The results showed that the landslide area was the highest within 1 km of the fault, reaching 1.09×10^6 m^2, accounting for 50.23% of the total landslide area. With the increase of the distance from the fault, the area of the landslide showed a decreasing trend, and almost no landslides occurred outside the range of 5 km from the fault.

6. Conclusions

Based on the 1 m high-definition UAV imagery after the Jiuzhaigou earthquake, this study proposed a support vector machine classification method to map the earthquake-triggered landslides accurately and automatically. By extracting road and villages from pre-seismic remote sensing imagery, the main error source in them was effectively eliminated. The landslides, roads, villages, and vegetations were clearly classified. Compared with the visual-interpretation results, the overall recognition accuracy of this method reached 99.89%. An accumulated landslide volume of 2.17×10^6 m^2 was identified in the Jiuzhaigou valley scenic and historic-interest area, owing to the use of UAV imagery with a resolution of 1 m. Finally, topographic factors were introduced to evaluate the spatial distribution of landslides.

The results showed that earthquake-triggered landslides were mainly distributed in the range of 2400–3000 m above sea level, in which the area density was highest in the range of 2400–2600 m above sea level. The area of earthquake-triggered landslides was significantly reduced outside this range. The slope gradient of the terrain where the landslides are located was mainly distributed in 35~40°, which was in agreement with the existing research results. In terms of slope aspect, earthquake-triggered landslides were concentrated in the range of the northern slope, but no clear relationship between the spatial distribution of the landslide body and the slope aspect was found. The landslides in the study area had an obvious

fault effect. As the distance from the fault increased, the number of the landslides showed a decreasing trend.

This study also demonstrated that high-resolution UAV imagery acquired in time after an earthquake can provide strong support to promptly acquire the landslide inventory map, and can become an effective means for an automatic and quasi-real-time mapping of landslides in the future, which would provide information support for subsequent landslide-risk assessment and a landslide-susceptibility study.

Author Contributions: Conceptualization, K.D. and X.F.; methodology, R.L. and B.G.; software, R.L.; investigation, F.L.; resources, B.G. and X.D.; writing—original draft preparation, R.L. and N.W.; writing—review and editing, K.D., X.S., B.G., and R.T.; funding acquisition, X.D. and K.D. All authors have read and agreed to the published version of the manuscript.

Funding: This work was funded by the National Key Research and Development Program of China (Project No. 2018YFC1505202), the National Natural Science Foundation of China (41941019), the State Key Laboratory of Geohazard Prevention and Geoenvironment Protection Independent Research Project (SKLGP2020Z012), the project on identification and monitoring of potential geological hazards with remote sensing in Sichuan Province (510201202076888) and the Everest Scientific Project at Chengdu University of Technology (2020ZF114103).

Conflicts of Interest: The authors declare no conflict of interest.

References

1. Fan, X.; Scaringi, G.; Korup, O.; West, A.J.; Westen, C.J.; Tanyas, H.; Hovius, N.; Hales, T.C.; Jibson, R.W.; Allstadt, K.E.; et al. Earthquake-Induced Chains of Geologic Hazards: Patterns, Mechanisms, and Impacts. *Rev. Geophys.* **2019**, *57*, 421–503. [CrossRef]
2. Xu, C. Landslide Seismology Geology: A Sub-discipline of Environ-mental Earth Science. *J. Eng. Geol.* **2018**, *26*, 207–222. [CrossRef]
3. Li, Q.; Zhang, J.F.; Luo, Y.; Jiao, Q. Recognition of earthquake-induced landslide and spatial distribution patterns triggered by the Jiuzhaigou earthquake in August 8, 2017. *J. Remote Sens.* **2019**, *23*, 785–795. [CrossRef]
4. Wang, H.; Zhang, L.; Yin, K.; Luo, H.; Li, J. Landslide identification using machine learning. *Geosci. Front.* **2021**, *12*, 351–364. [CrossRef]
5. Xu, C.; Dai, F.; Xu, X.; Lee, Y.H. GIS-based support vector machine modeling of earthquake-triggered landslide suscep-tibility in the Jianjiang River watershed, China. *Geomorphology* **2012**, *145–146*, 70–80. [CrossRef]
6. Liu, R.; Li, L.; Pirasteh, S.; Lai, Z.; Yang, X.; Shahabi, H. Performance quality of LR, SVM and RF for earthquake-induced landslides susceptibility mapping incorporating remote sensing imagery. *Arab. J. Geosci.* **2021**, *14*, 259. [CrossRef]
7. Li, Z.; Shi, W.; Myint, S.W.; Lu, P.; Wang, Q. Semi-automated landslide inventory mapping from bitemporal aerial photographs using change detection and level set method. *Remote Sens. Environ.* **2016**, *175*, 215–230. [CrossRef]
8. Dai, K.; Li, Z.; Xu, Q.; Burgmann, R.; Milledge, D.G.; Tomas, R.; Fan, X.; Zhao, C.; Liu, X.; Peng, J.; et al. Entering the Era of Earth Observation-Based Landslide Warning Systems: A Novel and Exciting Framework. *IEEE Geosci. Remote Sens. Mag.* **2020**, *8*, 136–153. [CrossRef]
9. Yang, X.; Chen, L. Using multi-temporal remote sensor imagery to detect earthquake-triggered landslides. *Int. J. Appl. Earth Obs. Geoinf.* **2010**, *12*, 487–495. [CrossRef]
10. Zhu, B.; Nie, Y. Using satellite remotely sensed data to monitor Yigong tremendous high-speed landslide. *J. Nat. Disasters* **2001**, 103–107. [CrossRef]
11. Behling, R.; Roessner, S.; Golovko, D.; Kleinschmit, B. Derivation of long-term spatiotemporal landslide activity—A multi-sensor time series approach. *Remote Sens. Environ.* **2016**, *186*, 88–104. [CrossRef]
12. Ding, H.; Zhang, M.; Zhu, W.; Zhang, T. High Resolution Remote Sensing for the Identification of Loess Landslides: Example from Yan'an City. *Northwestern Geol.* **2019**, *52*, 231–239. [CrossRef]
13. Li, Q.; Zhang, W.; Yi, Y. An Information Extraction Method of Earthquake-induced Landslide: A Case Study of the Jiu-zhaigou Earthquake in 2017. *J. Univ. Chin. Acad. Sci.* **2020**, *37*, 93–102. [CrossRef]
14. McKean, J.; Roering, J. Objective landslide detection and surface morphology mapping using high-resolution airborne laser altimetry. *Geomorphology* **2004**, *57*, 331–351. [CrossRef]
15. Martha, T.R.; Kerle, N.; Van Westen, C.J.; Jetten, V.; Vinod Kumar, K. Object-oriented analysis of multi-temporal pan-chromatic images for creation of historical landslide inventories. *ISPRS J. Photogramm. Remote Sens.* **2012**, *67*, 105–119. [CrossRef]
16. Dai, L.; Xu, Q.; Fan, X.; Chang, M.; Yang, Q.; Yang, F.; Ren, J. A Preliminary Study on Spatial Distribution Patterns of Landslides Triggered by Jiuzhaigou in Sichuan on August 8th, 2017 and Their Susceptibility Assessment. *J. Eng. Geol.* **2017**, *25*, 1151–1164. [CrossRef]
17. Deng, F.; Dou, A.; Wu, W.; Chen, Z.; Yuan, X. Rapid Investigation of Disaster Situation in Extreme Disaster Area ofJiu-zhaigou Earthquake in Sichuan Based on UAV Remote Sensing. *J. Catastrophol.* **2018**, *33*, 210–215. [CrossRef]

18. Keyport, R.N.; Oommen, T.; Martha, T.R.; Sajinkumar, K.S.; Gierke, J.S. A comparative analysis of pixel- and object-based detection of landslides from very high-resolution images. *Int. J. Appl. Earth Obs. Geoinf.* **2018**, *64*, 1–11. [CrossRef]
19. Fan, Q.; Ju, N.; Xie, M.; Zhao, J. Comparation of Geological Hazard Risks before and after Jiuzhaigou Ms7.0 Earthquake in 2017. *J. Seismol. Res.* **2019**, *42*, 419–427, 456. [CrossRef]
20. Karantanellis, E.; Marinos, V.; Vassilakis, E.; Christaras, B. Object-Based Analysis Using Unmanned Aerial Vehicles (UAVs) for Site-Specific Landslide Assessment. *Remote Sens.* **2020**, *12*, 1711. [CrossRef]
21. Pirasteh, S.; Li, J. Landslides investigations from geo-informatics perspective: Quality, challenges, and recommendations. *Geomat. Nat. Hazards Risk* **2016**, *8*, 448–465. [CrossRef]
22. Haneberg, W.C.; Cole, W.F.; Kasali, G. High-resolution lidar-based landslide hazard mapping and modeling, UCSF Parnassus Campus, San Francisco, USA. *Bull. Eng. Geol. Environ.* **2009**, *68*, 263–276. [CrossRef]
23. Xu, C. Preparation of earthquake-triggered landslide inventory maps using remote sensing and GIS technologies: Principles and case studies. *Geosci. Front.* **2015**, *6*, 825–836. [CrossRef]
24. Lu, P.; Qin, Y.; Li, Z.; Mondini, A.C.; Casagli, N. Landslide mapping from multi-sensor data through improved change detection-based Markov random field. *Remote Sens. Environ.* **2019**, *231*. [CrossRef]
25. Yi, Y.; Zhang, W. A New Deep-Learning-Based Approach for Earthquake-Triggered Landslide Detection from Single-Temporal RapidEye Satellite Imagery. *IEEE J. Sel. Top. Appl. Earth Obs. Remote Sens.* **2020**, *13*, 6166–6176. [CrossRef]
26. Pirasteh, S.; Li, J. Developing an algorithm for automated geometric analysis and classification of landslides incorporating LiDAR-derived DEM. *Environ. Earth Sci.* **2018**, *77*. [CrossRef]
27. Pirasteh, S.; Shamsipur, G.; Liu, G.; Zhu, Q.; Ye, C. A new algorithm for landslide geometric and deformation analysis supported by digital elevation models. *Earth Sci. Inform.* **2020**, *13*, 361–375. [CrossRef]
28. Chen, S.; Kang, Q.; Shen, Z.; Zhou, R. Landslide Detection Based on Color Feature Model and SVM inRemote Sensing Imagery. *Spacecr. Recovery Remote Sens.* **2019**, *40*, 89–98. [CrossRef]
29. Liu, P.; Wei, Y.; Wang, Q.; Chen, Y.; Xie, J. Research on Post-Earthquake Landslide Extraction Algorithm Based on Im-proved U-Net Model. *Remote Sens.* **2020**, *12*, 894. [CrossRef]
30. Xu, X.; Chen, G.; Wang, Q.; Chen, L.; Ren, Z.; Xu, C.; Wei, Z.; Lu, R.; Dong, S.; Shi, F. Discussion on seismogenic structure of Jiuzhaigou earthquake and its implication for current strain state in the sourtheastern Qinghai-Tibet Plataqu. *Chin. J. Geophys.* **2017**, *60*, 4018–4026. [CrossRef]
31. Li, Y.; Xing, C.; Chen, X. Analysis of the impact of the 2017 Jiuzhaigou Ms7.0 earthquake on nearby faults. *Earthquake* **2020**, *40*, 112–127. [CrossRef]
32. Ren, J.; Xu, X.; Zhang, S.; Luo, Y.; Liang, O.; Zhao, J. Tectonic Transformation at the Eastern End of the East Kunlun Fault Zone and the Seismogenic Mechanism of the 2017 Jiuzhaigou Ms7.0 Earthquake. *J. Geophys.* **2017**, *60*, 4027–4045. [CrossRef]
33. Peng, L.; Xu, S.; Mei, J.; Su, F. Earthquake-induced landslide recognition using high-resolution remote sensing images. *J. Remote Sens.* **2017**, *21*, 509–518. [CrossRef]
34. China Earthquake Network Center. Jiuzhaigou Earthquake. Available online: http://www.cea.gov.cn/publish/dizhenj/464/522/20171229103857324772935/index.html (accessed on 26 January 2018).
35. Chen, T.; Hu, Z.; Wei, L.; Hu, S. Data Processing and Landslide Information Extraction Based on UAV Remote Sensing. *J. Geo-Inf. Sci.* **2017**, *19*, 692–701. [CrossRef]
36. Rossi, G.; Tanteri, L.; Tofani, V.; Vannocci, P.; Moretti, S.; Casagli, N. Multitemporal UAV surveys for landslide mapping and characterization. *Landslides* **2018**, *15*, 1045–1052. [CrossRef]
37. Wang, L.; Zhao, L.; Liu, D. A Review on the Application of SVM in Hyperspectral Image processing. *J. Harbin Eng. Univ.* **2018**, *39*, 973–983. [CrossRef]
38. Yu, H.; Lu, Z. Review on landslide susceptibility mapping using support vector machines. *Catena* **2018**, *165*, 520–529. [CrossRef]
39. Zhang, R.; Ma, J. State of the Arton Remotely Sensed Data Classification Based on Support Vector Machines. *Adv. Earth Sci.* **2009**, *24*, 555–562. [CrossRef]
40. Shao, Y.; Lunetta, R.S. Comparison of support vector machine, neural network, and CART algorithms for the land-cover classification using limited training data points. *ISPRS J. Photogramm. Remote Sens.* **2012**, *70*, 78–87. [CrossRef]
41. Mazzoni, D.; Garay, M.J.; Davies, R.; Nelson, D. An operational MISR pixel classifier using support vector machines. *Remote Sens. Environ.* **2007**, *107*, 149–158. [CrossRef]
42. Bie, Q.; Zhao, C.; Peng, S.; Feng, Z. RS Information Extraction and Accuracy Evaluation Based on Multi-elements Data and Different Classify Method—A Case Study of the Eastern Section of Qilian Mountains. *Remote Sens. Technol. Appl.* **2009**, *24*, 551, 576–581. [CrossRef]
43. Huang, R.; Li, W. Research on Development and Distribution Rules of Geohazards Induced by Wenchuan Earthquake on 12th, 2008. *Chin. J. Rock Mech. Eng.* **2008**, *27*, 2585–2592. [CrossRef]
44. Huang, R. Mechanism and Geomechanical Modes of Landslide Hazards Triggered by Wenchuan 8.0 Earthquake. *Chin. J. Rock Mech. Eng.* **2009**, *28*, 1239–1249. [CrossRef]
45. Fan, X.; Scaringi, G.; Xu, Q.; Zhan, W.; Dai, L.; Li, Y.; Pei, X.; Yang, Q.; Huang, R. Coseismic landslides triggered by the 8th August 2017 Ms 7.0 Jiuzhaigou earthquake (Sichuan, China): Factors controlling their spatial distribution and implications for the seismogenic blind fault identification. *Landslides* **2018**, *15*, 967–983. [CrossRef]

46. Zhou, H.; Che, A.; Wang, L.; Wang, L. Investigation and mechanism analysis of disasters under Hokkaido Eastern Iburi earthquake. *Geomat. Nat. Hazards Risk* **2020**, *12*, 1–28. [CrossRef]
47. Zhang, S.; Li, R.; Wang, F.; Iio, A. Characteristics of landslides triggered by the 2018 Hokkaido Eastern Iburi earthquake, Northern Japan. *Landslides* **2019**, *16*, 1691–1708. [CrossRef]
48. Xu, Q.; Lie, W. Distribution of Large-scale Lnadslides induced by the Wenchuan Earthquake. *J. Eng. Geol.* **2010**, *18*, 818–826. [CrossRef]